Microstructure-Dependent Sodium Storage Mechanisms in Hard Carbon Anodes

Luis Kitsu Iglesias[1], Samuel D. Marks[2], Nikhil Rampal[3,4], Emma N. Antonio[2], Rafael Ferreira de Menezes[1], Liang Zhang[5], Daniel Olds[6], Stephen E. Weitzner[3,4], Kayla G. Sprenger[1], Liwen F. Wan[3,4], and Michael F. Toney[1,2,7]*

[1]Department of Chemical and Biological Engineering, University of Colorado Boulder, Boulder, CO 80309, USA

[2]Materials Science and Engineering, University of Colorado Boulder, Boulder, CO 80309, USA

[3]Materials Science Division, Lawrence Livermore National Laboratory, Livermore, CA 94550, USA

[4]Laboratory for Energy Applications for the Future (LEAF), Lawrence Livermore National Laboratory, Livermore, CA 94550, USA

[5]Phillips 66 Company, Energy Research & Innovation, Bartlesville, OK 74003, USA

[6]National Synchrotron Light Source II, Brookhaven National Laboratory, Upton, NY 11973-5000, USA

[7]Renewable and Sustainable Energy Institute, University of Colorado Boulder, Boulder, CO 80309, USA

BROAD CONTEXT

Sustainable energy storage is essential to support our transition to renewables and meet the increasing demand for energy. Sodium-ion batteries (NIBs) are attractive for grid-scale energy storage due to the abundance and low cost of sodium, sustainability of other battery components, and electrochemical performance. Hard carbon (HC) is the most promising anode for commercialization of NIBs. However, due to its structural complexity, the sodium storage mechanisms in HC and the dependence on microstructure remain unclear, limiting the development of high-performance anodes. Our research explores this complexity, unveiling how the HC microstructure dictates sodium storage. By elucidating these mechanisms, we bring crucial insights for engineering superior HC anodes that will enhance the efficiency and viability of NIB technology. This advancement propels the development of sustainable energy storage solutions and catalyzes our transition towards a more renewable-centric energy landscape.

Abstract

Hard carbon (HC) is a leading anode material for sodium-ion batteries, but its complex microstructure complicates understanding of sodium storage mechanisms. Using X-ray total scattering and density functional theory calculations, this study clarifies how HC's microstructural variations influence sodium storage across the slope (high potential) and plateau (low potential) regions of the potential-capacity curve. In the slope region, sodium initially adsorbs at high-binding energy defect sites and subsequently intercalates between graphene layers, adsorbing at low-binding energy defect sites, correlating with different slopes observed during initial sodiation. Initial irreversibility arises from sodium trapping at surface defects and solid electrolyte interface formation. In the plateau region, sodium simultaneously intercalates and fills pores, influenced by pore size, interlayer spacing, and defect concentration. HCs with larger pore sizes form larger sodium clusters. The proposed mechanism underscores the role of microstructure engineering in enhancing HC performance and advancing sodium-ion batteries for grid-scale energy storage.

1. Introduction

Sustainable battery technologies are central to meeting the growing demand for electric vehicles (EV) and grid-scale energy storage systems, which are critical for accommodating the intermittent nature of renewable energy sources.[1-2] Among the growing array of battery chemistries, sodium-ion batteries (NIBs) address many issues with lithium-ion battery technologies, including sustainability, safety, cost per energy density, and justice considerations related to critical mineral extraction and supply chains.[1-5] Leveraging abundant and environmentally benign materials for electrodes, NIBs offer a competitive low-cost alternative for inexpensive EVs and large-scale grid storage applications, which can be manufactured with existing fabrication facilities.[1-6] The advancement of NIB technology for a broader range of applications requires anode materials with higher capacity and reversibility. Meeting these demands, hard carbon (HC) has emerged as the most promising anode material for commercial NIBs due to its high capacity, electrochemical stability, low cost, and the abundance of its precursors (e.g., biomass). However, a general mechanism for sodium storage in HC – critical for widescale commercialization – has been elusive because of the complexity and sensitivity of storage mechanisms to HC microstructure.

The microstructure of HC is characterized by a disordered carbonaceous matrix of randomly oriented graphitic layers.[7-9] Structural features such as large graphene interlayer spacing,

curved graphitic domains, and high nanoporosity result in high reversible capacity and stable cycling performance.[7-11] The typical potential-capacity curve of HC exhibits two distinct electrochemical signatures: a sloping region at high potentials (~0.1–2.5 V vs Na/Na^+) and a plateau region at low potentials (~0–0.1 V vs Na/Na^+), as shown in Figure 1(a). During the first sodiation, the multiple slopes in the high potential region may correspond to distinct sodium storage processes with binding energy changes (as indicated by larger voltage drops during sodium insertion) that vary proportionally to the slope. The capacity and steepness of the gradients in the high voltage region also vary with pyrolysis temperature, indicating a dependence on the HC microstructure. The HC microstructure ultimately determines the total capacity and the relative capacities of the slope (with its different gradients) and plateau regions.[11]

The distinct features of the potential-capacity curve signify that multiple processes are needed to describe sodium storage along a single charge/discharge cycle. It has been established that sodium is incorporated into HC through three main processes: i) adsorption to defect sites at the surface of graphene layers, in graphitic layers, and pore walls, ii) intercalation between graphene layers, and iii) filling of nanopores.[12-25] Several studies using Raman spectroscopy and DFT calculations have correlated the slope capacity with the concentration of defects in graphene sheets, attributing the capacity in the slope region to sodium adsorption in defect sites, such as monovacancies, divacancies, and oxygen heteroatoms.[12-17] In contrast, using Raman spectroscopy and X-ray diffraction, other studies propose that sodium intercalation between graphene layers is the dominant storage mechanism within the slope region.[18-20] More complex mechanisms have also been proposed. Reddy *et al.*, using *in situ* Raman and DFT, suggested a four-stage sequential mechanism:[17] during the slope region, sodium ions first adsorb onto the active surface sites, then insert and adsorb onto intralayer defect sites before intercalating to fill the interlayers and, finally, filling the pores during the plateau region. Morikawa *et al.*, using *ex situ* wide- and small-angle X-ray scattering (SAXS), proposed a mechanism where sodium ions adsorb during the slope region, then intercalate at the end of the slope region and during the plateau region, and after the maximum intercalation capacity has been reached, sodium fills the pores at the end of the plateau region.[21] More recently, using DFT, X-ray diffraction and electrochemical measurements, Li et al. proposed a two-stage sequential mechanism where sodium ions adsorb in a range of defect sites, such as monovacancies, divacancies, and oxygen heteroatoms during the slope region, and then sodium fill the pores and form quasi-metallic clusters during the plateau region.[22] However, the specific

storage mechanisms corresponding to distinct capacity regions, as well as the sequence and details of the diffusion and storage steps remain under debate.[23] Further advancing HC anodes requires generalizable storage mechanisms for each voltage regime that can account for the range of HC microstructures encountered from different precursors (e.g., glucose, lignin, coconut shells, and synthetic resins) and synthesis conditions.

The discrepancies in reported sodium storage mechanisms reveal the characterization challenges posed by a multiplicity of HC microstructures. It is generally accepted that sodium adsorbs at defect sites during the slope region and fills the pores (clustering) during the plateau region.[12-17, 21-22] Yet, significant questions persist regarding the precise sequence for sodium adsorption in surface defect sites or intralayer defect sites, during what capacity region sodium intercalates, the cluster size dependence on pore size distribution, and whether storage processes occur in sequence or simultaneously as a function of potential. Experimental insight into these questions requires structural and chemical probes with sensitivity to the local structure. Recently, Stratford *et al.* used *operando* X-ray total scattering and ^{23}Na NMR to study both the local and average structure dynamics of the HC upon sodiation.[24] During the slope region, they show that sodium ions adsorb at a wide range of defect sites. During the plateau region, they conclude that sodium ions fill the pores and form metallic sodium clusters, consistent with our recent *operando* SAXS and X-ray absorption spectroscopy (XAS) measurements.[25] However, they did not observe changes in the graphene interlayer structure due to sodium intercalation, typically observed from the scattering peak that arises from the interlayer spacing which may have been obscured due to strong scattering from the electrolyte. Furthermore, they observed that differences in the average pore sizes of the two commercial hard carbons studied resulted in no significant difference in average sodium cluster size.

In this study, insights into the sodium storage mechanisms for different states of sodiation are obtained from X-ray total scattering measurements on three representative HCs with distinct microstructures. Subsequently, the local configurational states are evaluated by density functional theory (DFT) to provide atomic-level insights into the enthalpies and feasibility of sodium interactions within the HC structures. We find that HC microstructures prepared at higher pyrolysis temperatures, which exhibit larger average pore sizes, facilitate the formation of larger sodium clusters, thereby increasing capacity through sodium storage in the pores. Furthermore, we infer

that initial irreversibility primarily arises from sodium adsorption at high-binding energy surface defect sites, resulting in trapped sodium, and the formation of a solid electrolyte interface (SEI). The findings herein complement our previous report of simultaneous nanopore filling and intercalation during the low-voltage plateau region, with pore sizes that preferentially fill depending on microstructure as determined from *operando* SAXS and XAS measurements.[25] Finally, we differentiate sodium insertion between graphene layers via adsorption at intralayer defects from the conventional intercalation mechanism in which sodium adsorbs at the high symmetry points between graphene layers. We suggest that the comprehensive mechanism we propose for sodium storage in HC microstructures is generalizable and should be tested across different precursors and synthesis conditions to confirm its broader applicability.

2. Results & Discussion

2.1. Correlation between local structure and pyrolysis temperature.

Three HC structures prepared at different pyrolysis temperatures that resulted in distinct microstructures were studied with *ex situ* X-ray pair-distribution function (XPDF) analysis to determine the average local structure and sodium storage mechanisms. Samples prepared with pyrolysis temperatures of 1100°C, 1400°C, and 2000°C were investigated, denoted here as HC-1100, HC-1400, and HC-2000, respectively. To compare between different types of HC, we define a "state of sodiation" (SoS), where 0% SoS represents pristine HC and 100% represents the capacity at C/20 with a cutoff voltage of 0 V vs Na/Na^+. For the second cycle sodiation, the SoS is defined relative to the maximum capacity achieved during the first cycle sodiation. Each HC variant exhibits a unique potential-capacity curve. As depicted in Figure 1(a, b), HCs prepared at lower temperatures exhibit a higher slope capacity fraction, a smaller plateau capacity fraction, and a higher potential at the plateau onset compared to HCs prepared at higher temperatures.

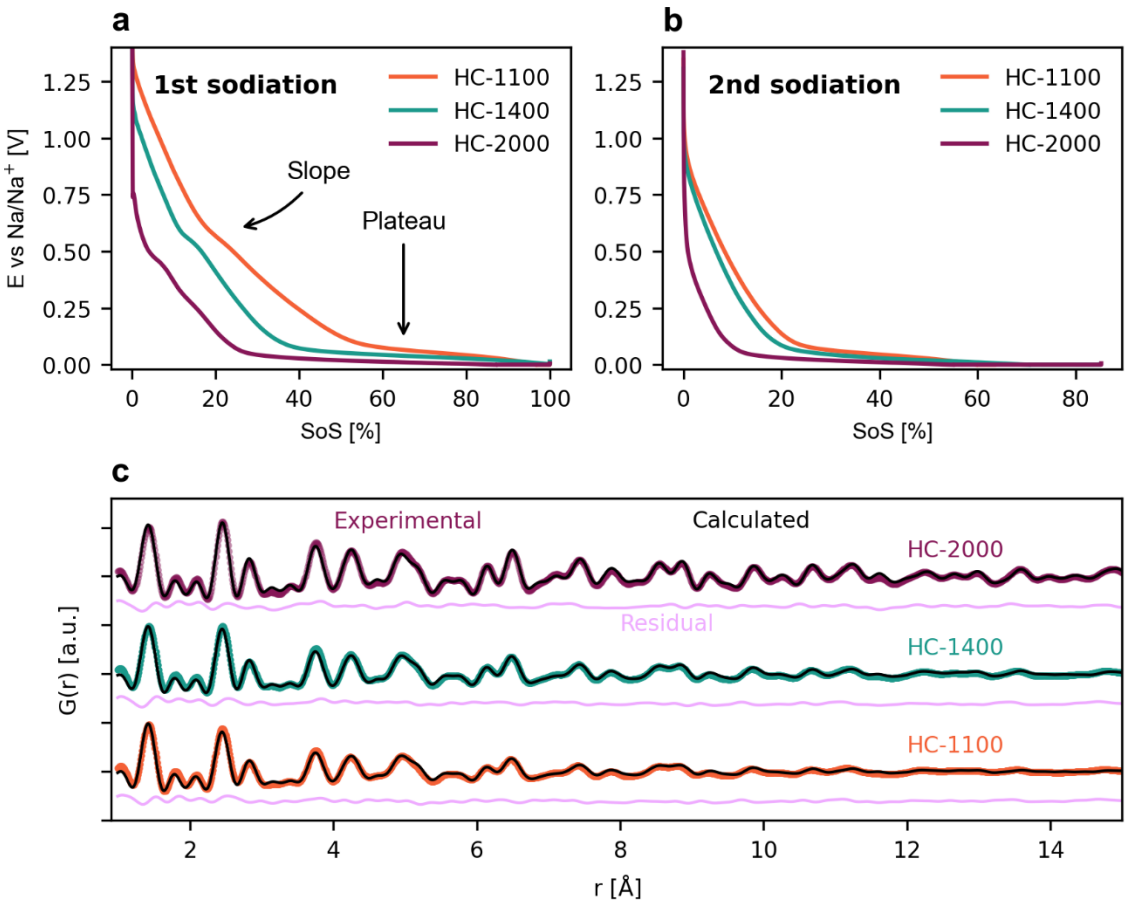

Figure 1. *Normalized capacity-potential curves of the three different HC structures at C/20 for a) the first sodiation and b) the second sodiation with the SoS relative to the first sodiation. The SoS at the end of the second sodiation is 63.7% for HC-1100, 81% for HC-1400, and 85.2% for HC-2000. c) X-ray PDFs (colored lines) fitted with the structural model described in this work (black lines). The difference curves (violet) are plotted beneath each fitted curve. The data and fits are offset for clarity.*

Two distinct gradients are present in the slope region: a steep gradient at high voltages followed by a shallower gradient at intermediate voltages preceding the plateau region. Lower temperature HCs display gradients that are more clearly differentiated, with both gradient regions showing higher capacity fractions than HCs prepared at higher temperatures (values stated in Figure S1). During the second sodiation (Figure 1(b)), there is a noticeable reduction in the slope capacity region for all HCs, indicating that sodiation in this region is more irreversible in comparison to the plateau region. This irreversibility is attributed to sodium adsorption during the first cycle at high-energy surface defect sites, where strong interactions between sodium and defect sites lead to sodium ion trapping, preventing their subsequent extraction. Filling the high-energy surface defect sites during the first cycle results in only one gradient starting at lower potentials during the second

sodiation. Additionally, electrolyte reduction at moderate potentials (~0.75 V vs. Na/Na^+) initiates the formation of a stable SEI during the first cycle, contributing significantly to irreversible capacity.[23, 26] The contributions from the slope and the plateau for the first and second cycles are quantified in Figure S1. The materials are ranked based on their performance, with HC-1400 exhibiting the highest initial capacity, followed by HC-1100, and then HC-2000. However, HC-2000 demonstrates the highest reversibility, followed by HC-1400, and then HC-1100. This ranking is consistent with HCs synthesized at lower temperatures having higher defect densities and presenting a higher initial irreversible capacity.

The performance differences exhibited by HC produced at different pyrolysis temperatures originate in their distinct microstructures and local chemical environments. To gain insight into the local order of the HCs with increasing pyrolysis temperature, X-ray total scattering measurements were performed to determine the pair distribution function (PDF). The PDFs (G(r), where r is the interatomic distance) derived from the Fourier-transformation of the corrected and normalized X-ray total scattering data are shown in Figure 1(c) for the three HCs. Consistent with prior observations,[24, 27-29] the peak positions closely match those observed from graphene layers. The lack of long-range order in HCs is evident from the damping of the PDF peaks with increasing r. The average coherence length of the graphitic domains is determined from this decay (Table 1). Qualitatively, longer-range ordering at higher temperatures is apparent from increased correlations at larger r. Furthermore, the absence of peaks in the PDF corresponding to graphene-sheet interlayer atomic correlations suggests significant turbostratic and positional disorder from one graphene sheet to the next.[27]

Further insight into the structural ordering is obtained by fitting structural models to the XPDF profiles. Here, we employ a simple small-box model consisting of a graphite unit cell with an expanded interlayer spacing to simulate the lower density of HC compared to graphite. High r correlations from the graphite are smoothed out by representing the diminishing long-range order with a spherical shape dampening function $\gamma(r, L_c) = 1 - \frac{3}{2}\left(\frac{r}{L_c}\right) + \frac{1}{2}\left(\frac{r}{L_c}\right)^3$ where L_c is the average coherence length and r is the interatomic distance. This dampening function is applied only when $r < L_c$. The lack of interlayer atomic correlations due to disorder between layers is simulated with artificially large interlayer atomic displacement parameters while maintaining the

microscopic density at the measured value. The in-plane interatomic distance (a), interlayer distance (d_{002}), L_c, and anisotropic displacement parameters (U_{11} and U_{33}, corresponding to in-plane and out-of-plane atomic displacements, respectively) are each refined. To maintain symmetry of the graphene layers, the following constraints are imposed: $U_{22} = U_{11}$ and $U_{12} = ½ U_{11}$. The resulting best-fits are included in Figure 1(c) with the experimental data and the parameters are reported in Table 1. Overall, we find good agreement between the measured and simulated G(r) profiles. The fitted PDFs reveal that increasing the pyrolysis temperature leads to enhanced local ordering within the graphitic layers. This is evident from the decrease in interlayer spacing and increase in coherence length of the graphitic domains. The observed increase in U_{33} with higher temperatures is attributed to a wider distribution of d_{002} spacings, which is correlated with a wider distribution of nanopores.[25] These results are consistent with observations reported for other HC materials.[28]

Table 1. HC microstructure parameters, including the in-plane lattice parameter (a), the interlayer spacing between graphene sheets (d_{002}), the average coherence length of graphitic domains (L_c), the in-plane anisotropic displacement parameter (U_{11}), and the out-of-plane anisotropic displacement parameter (U_{33}).

Sample	**a (Å)**	**d_{002} (Å)**	**L_c (Å)**	**U_{11} (Å^2)**	**U_{33} (Å^2)**
HC-1100	2.45	3.76	21	0.0025	0.23
HC-1400	2.45	3.72	25	0.0022	0.28
HC-2000	2.45	3.48	32	0.0021	0.36

Additionally, molecular dynamics (MD) simulations were performed to further explore the microstructural characteristics of pristine HC. Detailed in the SI (Figures S2-S4), these simulations, matching the experimental PDF, offer atomistic insights into porosity, and local structure. For example, we observe the presence of defects such as monovacancies, divacancies, five-membered rings, the curvature of graphene layers, and the layering of graphene sheets, providing a complementary perspective to the experimental results and delivering a more comprehensive understanding of the HC structure.

2.2. Sodium adsorption during the slope region

To understand the storage mechanisms during sodiation, *ex situ* XPDF measurements were made of the three HCs at states of sodiation spanning each electrochemical regime, shown in Figures S5-S14. We calculated the pair density function $\rho(r)$, which emphasizes short-range order and is related to G(r) by $\rho(r) = \frac{G(r)}{4\pi r} + \rho_0$, where ρ_0 is the average number density at each state of sodiation (see SI and Figures S15-S17). To highlight changes in the pair density function that arise during each storage process, the differential $\Delta\rho(r)$ is plotted (Figures S18-S23). By subtracting $\rho(r)$ obtained for an electrochemical region from the initial $\rho(r)$ in that region, $\Delta\rho(r)$ isolates new correlations that arise from changes in the local structure resulting from distinct electrochemical processes. Within the slope region, changes in the PDF result from the formation of new interatomic correlations (e.g., Na–C) and changes in existing pair correlation (e.g., C–C) distances. For example, Na–C correlations provide clues about whether sodium is adsorbed on the surface, intercalated between layers, or involved in other storage mechanisms based on the specific Na–C distances observed.

The total $\Delta\rho(r)$ exhibits a mixture of broad and sharp correlations (Figures 2(a,b)). Decomposing $\Delta\rho(r)$ into these two components enables the structural origin of each correlation to be individually examined. The broad components, $\Delta\rho(r)_{broad}$, consist of interatomic correlations that likely arise from Na–C and Na–Na correlations due to the highly disordered Na atoms within the HC structure. The sharp component, represented by $\Delta\rho(r)_{sharp}$, accounts for changes in the C–C bond distance upon sodiation. To obtain $\Delta\rho(r)_{broad}$, a Gaussian filter is applied to $\Delta\rho(r)$ with a kernel root-mean-square width (RMSW) of 0.3 Å (see SI for details). The sharp component is subsequently obtained with $\Delta\rho(r)_{sharp} = \Delta\rho(r) - \Delta\rho(r)_{broad}$. Examples of the deconvolution for the ends of the slope and plateau regions can be found in Figures S24 and S25, respectively, and deconvolution with other RMSW values of the Gaussian kernel can be found in the SI (Figure S26-S29). A RMSW of 0.3 Å best separates the Na–C and Na–Na correlations from the C–C correlations, based on the sharp component and the Na–C and Na–Na models that are discussed later. This RMSW value represents a compromise between a lower value, which might overlook relevant features, and a higher value, which could blur distinctions between different types of correlations.

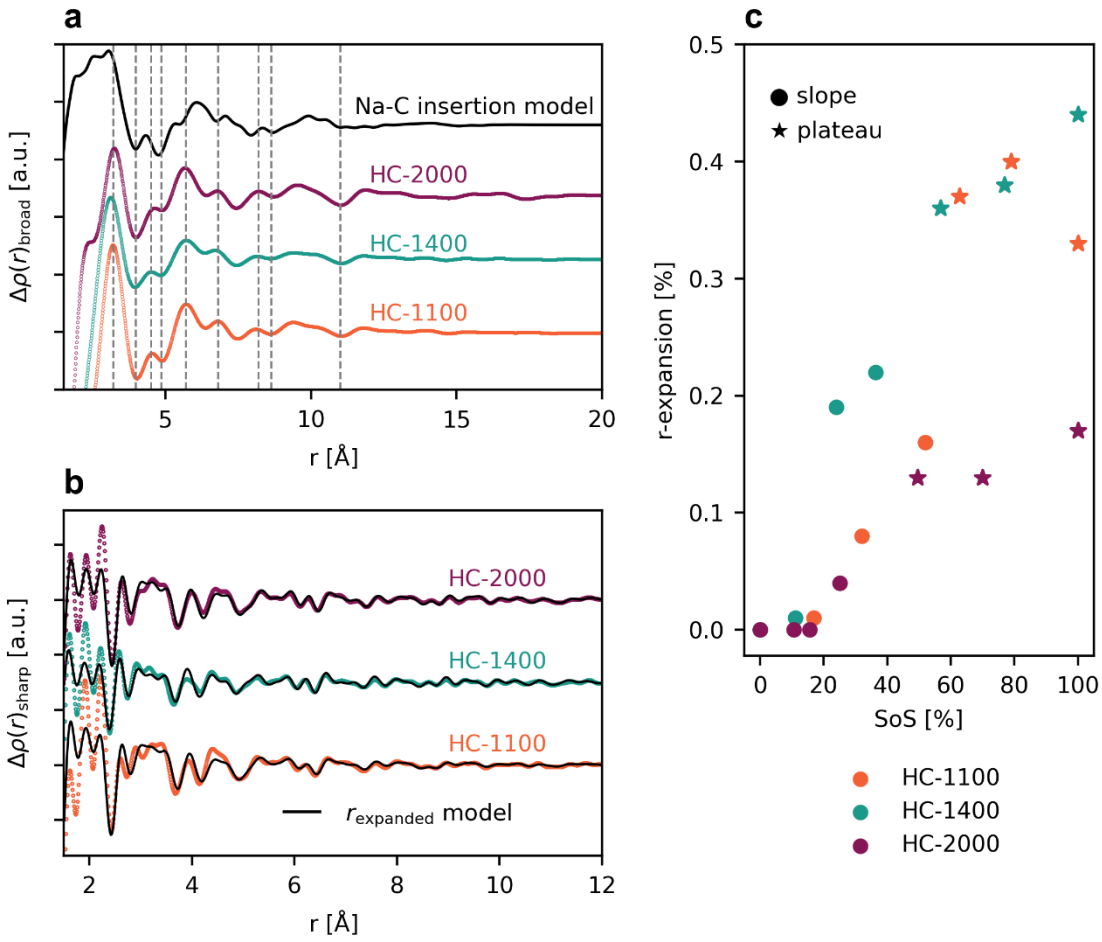

Figure 2. *a) Broad component of $\Delta\rho(r)$ for the end of the slope region for each HC, representing interatomic correlations that are broad in real space and appear during the slope region. The black curve represents the calculated Na–C correlations for sodium inserted between graphene layers using U_{iso} for sodium of 0.05 Å^2 (details in the SI). The gray dashed lines are used to compare the position of the main broad correlations between different HCs and the model. b) Sharp component at the end of the slope region for each HC with their corresponding fits of the expanded C–C correlations model in black. All curves have been offset for clarity. The curves without an offset and in absolute units can be found in the SI. c) Average r-expansion of the carbon bonds upon sodiation for all HCs. The filled circles are SoS in the slope capacity region whereas the stars are in the plateau capacity region. The end of the slope region is at 52% SoS.*

To clarify the sodium storage mechanism during the slope region, we employ small-box models of sodium insertion and adsorption in graphite (see SI) and validate these observations using DFT calculations. These models simulate the $\rho(r)$ containing only Na–C bonds and are compared to the broad component of the $\Delta\rho(r)$ measured in the slope region. In Figure 2(a), the experimental broad component is plotted for all HCs at the end of the slope region ($\Delta\rho(r) = \rho(r)_{end\ slope} - \rho(r)_{pristine}$). Similar correlations arise in the $\Delta\rho(r)_{broad}$ for each HC and qualitatively match the predicted Na–C correlations from sodium inserted between graphene layers,

indicated by the dashed vertical lines in Figure 2(a). The broad features are also consistent with simulated Na–C correlations for other models of Na near graphene layers, including sodium near monovacancies (Figures S30, S31). The rapid decay of $\Delta\rho(r)_{broad}$ for $r <$ ~2.5 Å coincides with the appearance of strong peaks at low r in $\Delta\rho(r)_{sharp}$, as seen in Figure 2(b). We suggest that the missing peaks in the broad component are "sharp" Na–C correlations due to Na atoms adsorbed at intralayer defect sites in graphene or intercalated between graphene layers. The sharpness of these peaks indicates specific, well-defined Na–C distances. We attribute the first peaks in the broad component (r ~ 3 Å) and sharp component (r ~ 1.9–2.2 Å) to these Na–C distances. Similar distances have been measured with differential PDF and predicted with DFT.[24, 30-31] For $r >$ ~8 Å, deviations in $\Delta\rho(r)_{broad}$ from the predicted Na–C insertion model may be caused by correlations from neighboring Na–Na atoms, the presence of defects such as monovacancies and divacancies, which will alter the relative intensities of the peaks, and C–C correlations that are broader in real space (*e.g.* disorder in the carbon matrix). However, the simple models for the broad component provide a reasonable match to the experimental data, indicating that a range of structures are present during sodium storage in the slope region, consistent with the literature.[24]

To account for the sharp C–C correlations that appear during cycling and are present in $\Delta\rho(r)_{sharp}$, a model is constructed by expanding the bond lengths ($r_{\text{expanded}} = r\,(1 + r_{multi})$) of $\rho(r)$ measured from pristine HC, and then subtracting $\rho(r_{\text{expanded}})$ from the pristine $\rho(r)$ (details in SI). This r_{expanded} model accounts for the average expansion of C–C bonds and is refined to fit the sharp component and obtain the average local expansion of C–C distances (Figure 2(b, c)). The r_{expanded} model provides a reasonable match to the experimental sharp component above 2.5 Å (Figure 2(b)), indicating that the narrow correlations arising during the slope region can largely be attributed to expanded C–C distances. We note that this model is not sensitive to other C–C and/or Na–C sharp correlations that may be present, such as local distortions in the carbon matrix, sodium interactions at specific defect sites, and higher-order correlations. For example, the $r_{expanded}$ model fails to capture correlations around r ~ 1.9–2.2 Å. These correlations are present in the Na–C insertion model, but not in the experimental broad component (as noted above). Thus, we propose that the sharp peaks at r ~ 1.9–2.2 Å are Na–C correlations arising from ionic sodium located near graphene layers, consistent with sodium adsorption at defect sites.

Figure 2(c) shows the r expansion derived from fits to $\Delta\rho(r)_{sharp}$ for different states of sodiation spanning the slope and plateau regions for all HCs. For each HC, the intralayer C–C bonds expand during the slope region, ultimately stabilizing in the low voltage plateau region. Similar C–C expansion values have been reported following sodium insertion in HC and potassium intercalated in graphite.[29, 32] The trend in C–C expansion within the slope region has been rationalized by sodium adsorption at intralayer graphene defect sites. Raman spectroscopy and X-ray diffraction studies indicate that the transfer of charge-compensating electrons to π* antibonding orbitals in graphite layers that accompanies alkaline metal adsorption results in weakening and expansion of the C–C bond.[19, 32-33] HC-2000 exhibits smaller C–C expansion compared to the lower temperature HCs. This can be rationalized by HC-2000 having the lowest overall defect concentration which results in lower sodium adsorption and thus less transfer of electrons to the carbon.[25] Instead, more electrons transfer to the sodium, which is consistent with our previous XAS data that shows a reduced sodium oxidation state.[25] Within the plateau region, the C–C bond lengths stabilize as open adsorption sites deplete and additional sodium ions transport to pores where cluster formation begins. In this regime, the transfer of charge-compensating electrons follows the condensation of sodium ions into growing clusters in the pores.

Analysis of the broad and sharp components of the XPDF collected from within the slope region suggests a potential mechanism involving the insertion of sodium into the HC and the local expansion of C–C bonds following sodium adsorption. The specific distribution of Na–C correlations depend on the HC microstructure, with possible Na–C environments including ionic sodium located near graphene surfaces, between graphene layers, and near point defects within graphene layers such as vacancies or substitutional impurities. Note that these models are agnostic to other changes in the carbon structure beyond the expansion of C–C distances, for example, the possible local environments created by sodium insertion into the complex HC structures or Na–Na correlations. More complex modeling, such as reverse Monte Carlo (RMC) refinement, may reveal a wider distribution of local environments created by sodium insertion. However, such models often struggle to provide a unique fit to the data due to the large number of refined atomic positions.

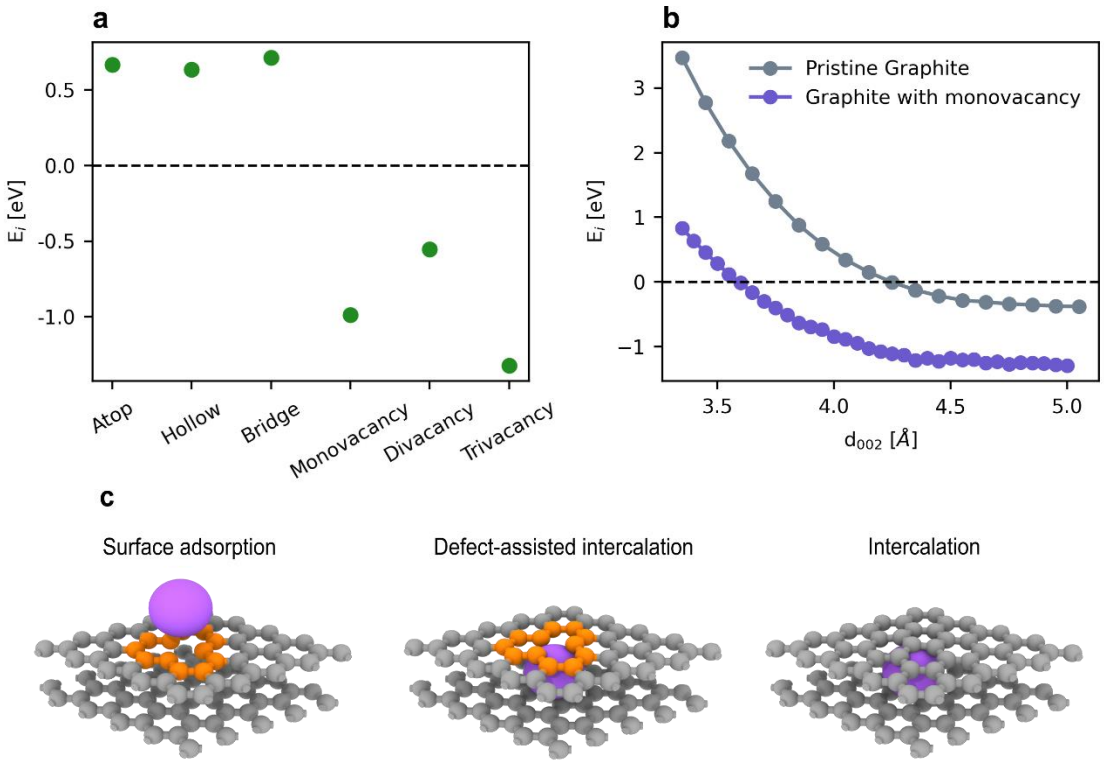

Figure 3. *a) Sodium adsorption energies (E_i) of sodium on different surface and defect sites. Schematic of these structures are shown in Figure S32. b) Sodium incorporation energies of sodium intercalated in defective graphite (purple) and sodium intercalated in pristine graphite (gray), for different d(002) spacing values. c) DFT simulated structures for sodium incorporation via surface adsorption at a monovacancy site, defect (monovacancy)-assisted intercalation, and bulk intercalation in pristine graphite. The calculated sodium incorporation energies (E_i) indicate that surface adsorption is thermodynamically most favorable, followed by defect-assisted intercalation and, lastly, conventional intercalation. Gray spheres represent carbon atoms, and purple spheres represent sodium atoms. Orange spheres highlight the carbon atoms surrounding a monovacancy. Two additional graphene layers are hidden for illustration purposes.*

Using DFT calculations, we further elucidate how surface defects alter sodium incorporation energies. At the atomistic scale, surface adsorption at the atop, bridge and hollow sites of pristine graphene are energetically unfavorable (Figure 3(a), Figure S32). We find that sodium adsorption at each of these sites is energetically similar: 0.67, 0.63 and 0.71 eV at the atop/bridge/hollow sites, respectively. However, in the presence of monovacancies or divacancies, the sodium adsorption energies are substantially lowered, -0.99 eV and -0.55 eV, respectively, indicating that interactions between sodium and defected carbon are most favored. This observation, consistent with previous work,[13,17] underscores the importance of defects in facilitating sodium adsorption. In addition, DFT calculations reveal how intralayer defects, specifically monovacancies, alter sodium incorporation energies in expanded d_{002} graphite. As shown in Figure 3(b), the presence of intralayer defect sites makes sodium intercalation more favorable. We define this as

the "defect-assisted intercalation" mechanism, in which intercalated sodium ions are coordinated by intralayer defect sites, consistent with previous characterization of defect environments.[17] This mechanism differs from conventional intercalation due to the significantly stronger electrostatic coordination provided by the charge-deficient carbon at defect sites (Figure 3(b,c)). Our DFT results demonstrate that the minimum favorable post-intercalation d_{002} spacing for defect-assisted intercalation is ~3.6 Å, compared to ~4.2 Å for conventional intercalation. This highlights how defects play a pivotal role in lowering the energy barrier for sodium incorporation, thereby enhancing intercalation in defected carbon structures.

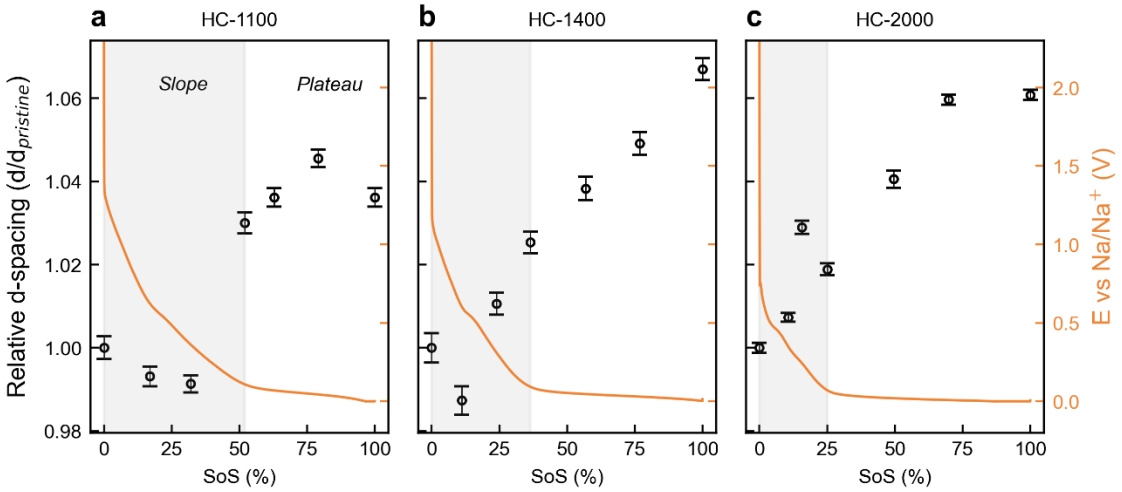

Figure 4. *Average relative interlayer distance upon sodiation derived from deconvolution analyses of the WAXS patterns (see SI) for a) HC-1100, b) HC-1400, and c) HC-2000. The gray shadow highlights the sloping region in the potential curves.*

To examine the impact of sodium insertion on the average interlayer spacing for each HC, the relative changes in interlayer spacing are determined from wide-angle X-ray scattering (WAXS) measurements capturing the (002) and (100) reflections during sodiation. The (002) reflection was fitted to determine the interlayer spacing, with the detailed fits provided in Figures S38-S57. Figure 4 shows systematic shifts in the interlayer spacing throughout the sodiation process across all HCs. For HC-1100 and HC-1400, during the first gradient of the slope region, the interlayer spacing decreases slightly due to localized contraction instigated by sodium adsorption at defect sites on the HC surface, observable by the high surface area. Subsequently, during the second gradient of the slope region, the interlayer spacing increases for all HCs. For HC-1100, this increase occurs between 32% and 52% SoS. This phenomenon, along with the increase in the C-C bond distance (Figure 2(c)), DFT calculations (Figure 3(b, c)), and supporting evidence from

Raman studies,[17] aligns with the "defect-assisted intercalation" mechanism. It is important to note that both "defect-assisted intercalation" and conventional intercalation mechanisms result in an increase in d_{002}, making it challenging to distinguish between these two mechanisms based on d_{002}. Our DFT calculations confirm that the defect-assisted intercalation is energetically more favorable than conventional intercalation, which explains why defect-assisted intercalation occurs at higher potential in the potential-capacity curve. The wide range of intralayer defect sites with varying adsorption energies results in a sloping potential region. During the plateau region, the average interlayer spacing increases for each HC, signifying continued intercalation of sodium ions between the graphene layers. Note that for HC-2000, no decrease in the d-spacing is observed in the slope region; we speculate that this is because HC-2000 has fewer available surface defects and a lower surface area, consistent with the comparatively small initial slope region (below 5% SoS).[25] Thus, sodium ions must intercalate to reach intralayer defect sites, resulting in observed increase in d_{002}.

Integrating our simplified models of sodium insertion with the expansion of C–C bonds, the changes in d-spacing, and DFT calculations, we propose a sequential adsorption mechanism occurring during the slope region. Initially, during the steepest part of the slope region, sodium ions adsorb to high-binding energy defect sites, such as monovacancies, on the surface of HC, as evidenced by DFT calculations (Figure 3(a)) and the decrease in d-spacing upon initial sodiation. This initial adsorption results in the localized expansion of C–C bonds due to the filling of π^* antibonding orbitals.[32-33] Localized interactions between adsorbed Na and C are evident in the $\Delta\rho(r)$ from adsorption models and are consistent with DFT calculations and Raman spectroscopy.[13, 17, 34] Subsequently, sodium ions adsorb at lower binding energy surface defect sites, such as divacancies.[17] As sodiation continues toward lower voltages within the slope region, sodium ions begin to transport and intercalate between graphene layers, coordinated by intralayer defect sites, causing the average interlayer spacing to increase, consistent with Na–C correlations seen in $\Delta\rho(r)_{broad}$. Sodium ions eventually reach the pores and adsorb at defect sites in the pore walls. Lower defect concentrations in HC produced at high pyrolysis temperatures result in the smaller slope capacities observed in the potential-capacity curves. The observed increase in average interlayer spacing during the slope region has previously been attributed to conventional intercalation,[20] characterized by reversible insertion of ions into the interlayer sites of a host lattice. However, we propose that sodium ions must first insert between the graphene layers to access intralayer

defect sites, leading to an increase in interlayer spacing. Finally, we suggest that sodium adsorption at the surface defect sites is most likely to be irreversible, causing capacity losses during initial cycles. This is evidenced by the decrease in the slope capacity region during the second sodiation, the reduction in high voltage storage sites, the absence of two gradients in the slope region, and favorable sodium-ion adsorption energies.

From the XPDF analysis presented above, we deduce that sodiation within the slope region occurs over a broad distribution of storage sites that characterize sodium adsorption and the corresponding changes in the HC structure. These storage sites are filled as the electrochemical reactions proceed, with certain chemical environments being more energetically favorable and, consequently, manifesting earlier in the sequence. The slope in the potential-capacity curve reflects the contribution of various sites to the overall sodium storage, with the first and steeper gradient indicative of adsorption at surface defect sites (Figure 3 and Figure 4) and the subsequent and shallower gradient representing sodium adsorption at intralayer defect sites, *e.g.* the defect-assisted intercalation process described above. It is noteworthy that while some high-binding energy storage sites may initially show greater sodium uptake due to their higher reactivity and thermodynamically favorable nature, desorption from these sites is consequently less favorable, as observed by the decrease in the slope capacity region during the second cycle (Figures 1(b) and S1). This emphasizes the importance of balancing thermodynamic and kinetic considerations when designing sodium storage systems.

2.3. Sodium intercalation and pore filling during the plateau region

To understand the changes occurring during the plateau region, $\Delta\rho(r)$ is again deconvoluted into broad and sharp components. These are shown in Figure 5, subtracting fully sodiated HCs with those sodiated to the end of the slope region. New correlations arising during the plateau region observed in the broad component of the $\Delta\rho(r)$ in Figure 5(a) are attributed to the formation of sodium metal clusters with average radii of 8, 10, and 16 Å for HC-1100, HC-1400, and HC-2000, respectively. The cluster radii are evident from the spatial extent of the correlations at larger interatomic distance *r*. Sodium metal clusters were simulated as spherical clusters in a BCC arrangement with introduced disorder. Figure S33 shows simulated $\rho(r)$ for clusters of varying radii, while Figure S34 provides a detailed comparison of correlations at large interatomic distances across HCs. The observed Na–Na correlations are consistent with pore filling and subsequent

cluster formation during the plateau region with larger clusters forming in HCs prepared at higher pyrolysis temperatures.[25] Furthermore, the size of the clusters closely matches the largest pore sizes that are filled for each HC,[25] suggesting that the correlations observed in the broad component of the $\Delta\rho(r)$ originate from the largest sodium clusters. Although PDF analysis is primarily sensitive to pair correlations arising from the largest clusters, we expect a cluster size distribution for each HC that matches the distribution of filled pore sizes.

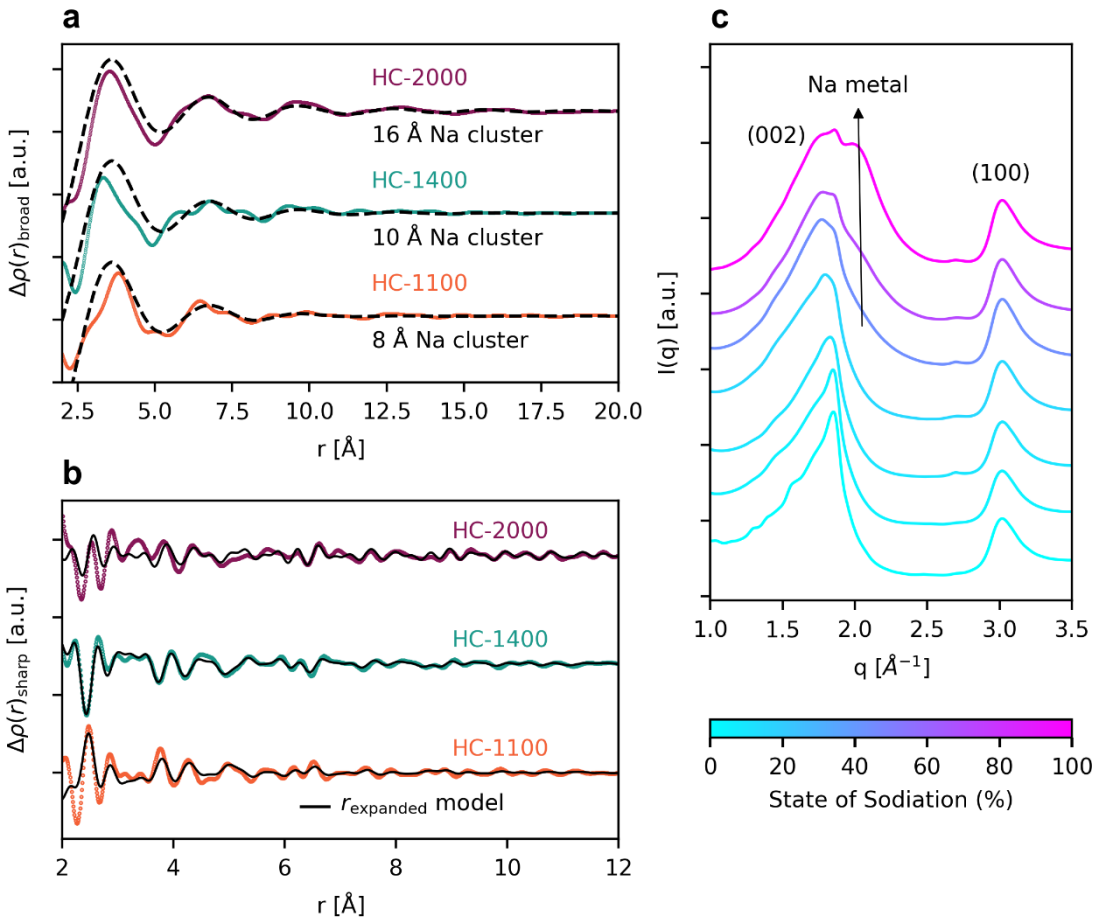

Figure 5. *a) Broad component of the $\Delta\rho(r)$ for all HCs for the end of the plateau region. The black dashed curves represent the calculated Na-Na correlations for sodium metal clusters (U_{iso} = 0.5) of 16, 10, and 8 Å radius, corresponding to HC-2000, HC-1400, and HC-1100, respectively. The same plot without the sodium clusters models to enhance the clarity of the experimental data shown in Figure S33. b) Corresponding sharp component for all HCs with their corresponding fits of the expanded C–C correlations model in black. All curves have been offset for clarity. The curves without an offset and in absolute units can be found in the SI. c) WAXS patterns for HC-2000. Note the appearance of a new peak during the plateau region, corresponding to sodium metal, annotated by an arrow.*

In Figure 5(b), we show that fitting $\Delta\rho(r)_{sharp}$ to the r_{expanded} model adequately accounts for the sharp component during the plateau region. In Figure 2(c), we show that the C–C bond

distance increases at the start of the plateau region and remains unchanged during the plateau region, suggesting no further reduction of the carbon during the plateau region. In contrast, as the HCs approach full sodiation, there is significant metallic sodium cluster formation which requires electron transfer to the sodium.

Finally, WAXS (Figures 5(c), S36, S37) unveils a distinctive peak near q = 2.06 $Å^{-1}$ at full sodiation for all HCs, corresponding to BCC Na metal (110) peak and consistent with the literature,[21] providing definitive evidence of the crystalline and metallic nature of the sodium clusters. Together with the increasing interlayer spacing observed during the plateau region (Figure 4) from WAXS, and the filling of the pores during the plateau region from *operando* SAXS, this suggests simultaneous intercalation and pore filling with the formation of clusters during the plateau region. We hypothesize that the Na–Na correlations for sodium clusters in the $\Delta\rho(r)_{broad}$ in Figure 5(a) obfuscate the weaker Na–C correlations for sodium intercalation due to the stronger scattering from Na–Na pairs compared to Na–C.

Our study indicates that during the plateau region, there is simultaneous sodium intercalation and pore filling, with the relative contribution of these mechanisms depending on the HC microstructure. At lower pyrolysis temperatures, the combination of larger interlayer spacing, lower volume fraction of pores, and smaller pore volumes results in Na intercalation being the dominant storage mechanism.[25] A larger contribution from intercalation is consistent with fewer pores filling during the plateau, as we previously reported.[25] Furthermore, smaller sodium clusters formed at lower pyrolysis temperatures are consistent with the preferential filling of smaller pores.[25] At higher pyrolysis temperatures, smaller interlayer spacing and larger volume fraction and pore volumes make it more difficult for sodium ions to intercalate. This produces a higher fraction of sodium stored in closed pores as metallic clusters, consistent with the Na–Na correlations in $\Delta\rho(r)_{broad}$ as well as our previous findings from XAS and *operando* SAXS experiments.

2.4. Sodium storage mechanisms in hard carbon anodes

Combining insights from the local structure characterization and DFT calculations presented here with our previous *operando* SAXS, XAS, Raman spectroscopy,[25] and other studies in the literature,[12-17, 21-24] we propose a new 3-stage general mechanism for sodium storage in HC anodes: (1) surface adsorption, (2) defect-assisted intercalation, and (3) simultaneous intercalation/pore filling. This mechanism, shown schematically in Figure 6, clarifies the sequence of storage processes, the coexistence of mechanisms within capacity regimes, the influence of microstructure on sodium cluster size, and the role of defect-assisted intercalation versus conventional intercalation.

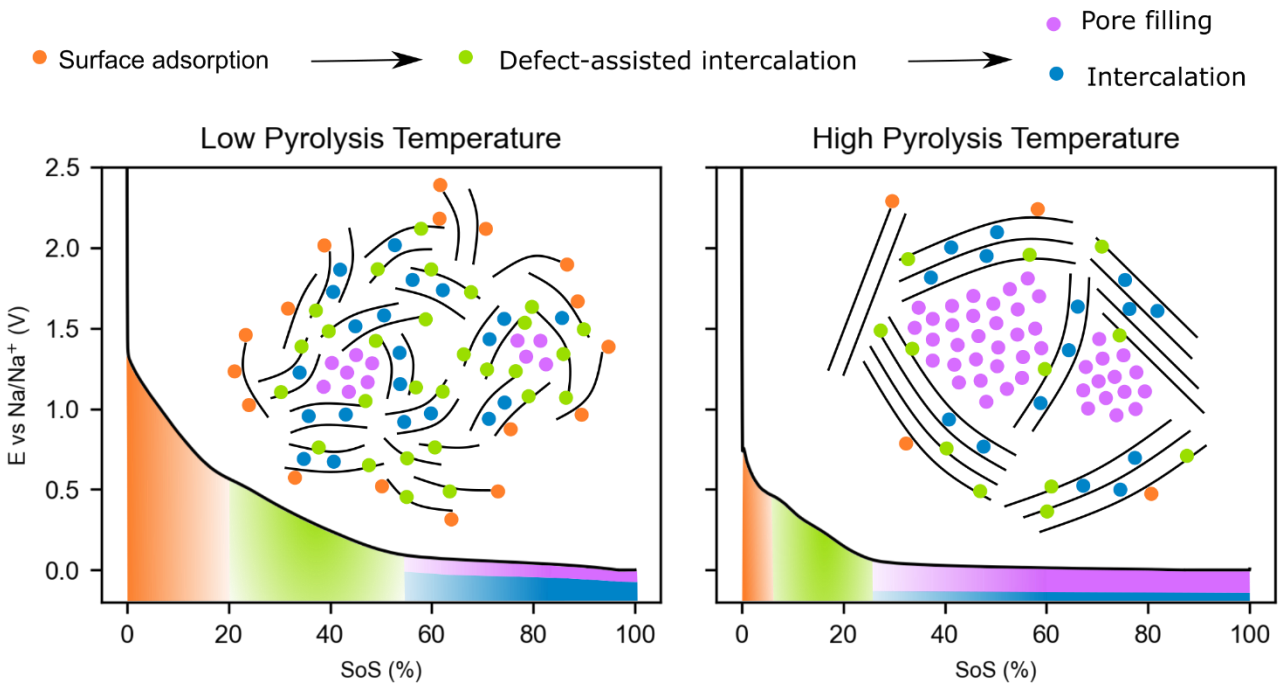

Figure 6. *Schematic representation of the microstructure-dependent sodium storage mechanism for hard carbons synthesized at different pyrolysis temperatures. The circles represent sodium atoms whereas the black lines represent graphene layers. The orange circles represent sodium ions adsorbed in surface defect sites and edges, the green circles represent sodium ions adsorbed in defect sites that are in between graphene layers and in pores. The blue and purple circles represent sodium atoms intercalating between graphene layers and filling and clustering in the pores, respectively.*

At first sodiation, initial sodium adsorption occurs at highly reactive surface defect sites of HC, resulting in a high voltage slope region due to a wide distribution of adsorption energies. During the second gradient of the slope region, sodium ions insert between the graphene layers to reach intralayer defect sites and defect sites within pore walls, producing an increase in interlayer spacing. This mechanism describes the sodium insertion required to reach defect sites, or "defect-assisted intercalation", which is distinct from the conventional intercalation mechanism. The two

sequential storage mechanisms that occur during the slope region are corroborated by the observed interlayer spacing shift, expansion of C–C bonds, $\Delta\rho(r)_{broad}$, and DFT calculations which indicate sodium adsorption and insertion in the layers. Within the plateau region, sodium ions simultaneously intercalate between graphene layers and fill the pores with the formation of metallic sodium clusters in the pores. The ratio between pore filling and intercalation, as well as which pores are preferentially filled, depends on the specific HC microstructure. At higher pyrolysis temperatures, larger pores are available and preferentially fill through the formation of larger sodium clusters.[25] For these HC microstructures, pore filling is the dominant sodium storage mechanism when compared with intercalation.

To conclude, sodium storage in hard carbon occurs in 3 different stages, with the last stage having two processes occurring simultaneously: adsorption on reactive surface sites, insertion and adsorption at intralayer defect sites and on pore walls, and intercalation between layers and nanopore filling occurring simultaneously. Based on these findings, we suggest the following design strategies to maximize the sodium storage capacity of HC. The presence and speciation of defects within graphitic domains are crucial for initiating sodium insertion and pore filling. Moreover, the sodium insertion capacity in the slope region depends on the defect concentration and defect type. However, the defect concentration should not be too high because of the high binding energy of sodium on these sites, which may be responsible, in part, for the irreversible capacity by trapping adsorbed sodium. Additionally, the formation of a SEI during the first cycle contributes significantly to irreversible capacity due to the reduction of electrolytes at specific moderate potentials. The irreversible adsorption at high-energy surface defects and the formation of the SEI are consistent with the lower electrochemical reversibility observed in the slope region compared to the plateau region for all HCs (Figure 1b and S1). The capacity in the plateau region depends on the nanopore volume and distribution and interlayer spacing. Hence, the capacity in this region can be increased by optimizing the pore size distribution while maintaining an interlayer spacing that does not inhibit diffusion. To improve the capacity and initial Coulombic efficiency of HC materials, several design strategies should be considered: morphological engineering, pore engineering, defect engineering, heteroatom engineering, and electrolyte engineering. These approaches can collectively enhance the capacity and reversibility of sodium storage in HC. This study not only sheds new light on the intricate sodium storage mechanisms in HC anodes but also provides a robust

framework for understanding and optimizing the performance of sodium-ion batteries for grid-scale energy storage, low-cost, and low-speed EV applications.

3. Experimental Procedures

3.1. Materials

Three different hard carbons were provided by Phillips 66 Company. To prepare the samples, a refinery heavy stream was converted into an oxidized intermediate. HC-1100ºC and HC-1400ºC were further carbonized in a laboratory tube furnace (SentroTech) by holding at the desired set point (1100ºC and 1400ºC respectively) for 2 h with a nitrogen flow at 500 sccm. HC-2000ºC was carbonized in a vacuum graphitization furnace (Centorr Vacuum Industries) at 2000ºC for 15 min.

3.2. Electrochemical measurements

The working electrodes were prepared by mixing 90 wt% of HC, 5 wt% of carbon Super P (Alfa Aesar ≥99%) as a conducting material, and 5 wt% of polyvinylidene (PVDF, MSESupplies ≥99.6 %) as a binder in N-Methylpyrrolidone (NMP, MSESupplies ≥99.9%, anhydrous). The resulting slurry was cast on aluminum foil (MTI ≥99.3%) using a 200 µm doctor blade. The film was first dried at 100ºC using a hot-plate for approximately one hour and then vacuum-dried overnight at 100ºC to fully remove NMP. The electrode film was punched into 14 mm diameter disks for the coin cells.

The coin cells (CR2032-type) were assembled using the HC electrode as a working electrode and metallic sodium (Alfa Aesar 99.8%) as a counter electrode. The separator used was a glass micro-fiber filter (Whatman, GF/B, 0.68 mm thickness). The electrolyte was 1 M NaPF6 (Alfa Aesar ≥99%) in ethylene carbonate (Sigma-Aldrich ≥99%, acid <10 ppm, H2O<10 ppm) and dimethyl carbonate (Sigma-Aldrich ≥99%, acid <10 ppm, H_2O<10 ppm) (1:1 vol%). The cells were galvanostatically charged and discharged in a voltage range of 0–2 V versus Na+/Na using a potentiostat (Biologic VSP-300) at a current density of 15 µA mg^{-1} at room temperature. At the end of the discharge the voltage was held constant at 0 V until the current decayed to 1.5 µA mg^{-1}.

Coin cells were discharged to desired voltage points, immediately disconnected, and disassembled inside an Ar-filled glove box (<0.5 ppm H_2O, <1 ppm O_2). The sodiated HC was scraped off the aluminum foil, and then stored and sealed with epoxy in 1.5 mm OD quartz capillaries to prevent both O_2 and moisture exposure. The capillaries were transported to the NSLS-II and measured.

3.3. X-ray pair distribution function

X-ray total scattering of the sodiated electrodes was measured at the NSLS-II (Brookhaven National Laboratory) at beamline 28-ID-1. These measurements were performed at an X-ray energy of 74.465 keV (0.1665 Å) with a 2D PerkinElmer detector (2048 x 2048 pixels, 200 x 200 μm^2 each) placed 28.3 cm from the sample. The electrodes were measured in sealed 1.5 mm quartz capillaries for a total exposure time of 1230 s (30s scan x 41 scans) per sample under ambient temperature and pressure. A diode mounted on the beamline was used to measure the X-ray transmission, which was corrected for dark current. Samples were monitored for beam damage by alternating measurement positions and exposure times. Polarization and geometric corrections were applied to the raw data, which was reduced using the pyFAI package. Data was corrected by transmission and the scattering from the empty capillary was subtracted from the sample measurements. PDFGetX3 was used to obtain the S(q) and pair distribution function in G(r) space, with corrections for sample self-absorption, detector oblique incidence and Compton and Laue scattering. The q-range for the Fourier transform was q_{min} = 0.26 $Å^{-1}$ to q_{max} =21.2 $Å^{-1}$. PDFgui was used to refine the G(r) for the pristine HCs and to simulate the G(r) for the different models. CeO_2 was used as a calibrant and it was refined to obtain the q_{damp}=0.027 $Å^{-1}$ and instrumentation broadening of q_{broad}=0.015 $Å^{-1}$ from beamline (Figure S34).

3.4. DFT calculations

Spin-polarized DFT calculations were conducted using the Vienna Ab-initio Simulation Package (VASP) to evaluate sodium adsorption behavior in pristine and defected graphene/graphite models, as proxies of hard carbon electrodes with various types of local defects.[35-39] The carbon electrode surfaces were modeled as both monolayer and bilayer graphene sheets. For simulating bulk-like intercalation, the graphite model was employed. Semi-local Perdew-Burke-Ernzerhof (PBE) exchange-correlation functional, and a PAW representation of the wavefunction with a kinetic energy cutoff of 450 eV was used in all simulations.[40] The Brillouin integration was performed using a 3x4x1 **Γ**-centered Monkhorst-Pack grid.[41] To capture the long-range dispersion forces between the graphene layers, an empirical DFT-D3 (BJ) energy correction was added [42] and the simulation cells were fully relaxed to reach the energy and force thresholds of 10^{-6} eV and 10^{-5} eV/Å.

The sodium incorporation energy (E_i) is evaluated using the following equation:

$$E_i = E_{Na+C} - E_C - n\,E_{Na}$$

Where E_{Na+C} denotes the total energy of the carbon electrode with the incorporated sodium, either on the surface or between the graphene layers, E_C is the energy of the sodium-free graphene/graphite sheet, E_{Na} is the energy of a metallic sodium (i.e. referenced to sodium metal), and n is the number of sodium atoms incorporated. To calculate E_i as a function of d_{002}-spacing, initial graphite structures with various d-spacings are generated, and a sodium ion is embedded within the interlayer. The graphite layers in contact with the sodium ion are fixed in the z-coordinate, while the other interlayers are allowed to relax.

Acknowledgements

The PDF research used beamline 28-ID-1 (PDF) of the National Synchrotron Light Source II, a US Department of Energy (DOE) Office of Science User Facility operated for the DOE Office of Science by Brookhaven National Laboratory under contract no. DE-SC0012704. L.K.I, S.D.M, E.N.A. and M.F.T. acknowledge support from the College of Engineering and Applied Science, the Materials Science Program and the Department of Chemical and Biological Engineering at University of Colorado Boulder. The computational portion of the work was performed under the auspices of the U.S. Department of Energy by Lawrence Livermore National Laboratory under contract number DEAC52-07NA27344 and the authors acknowledge the computing support from the Computing Grand Challenge program sponsored by Lawrence Livermore National Laboratory.

Author Contributions

L.K.I., E.N.A., and M.F.T. conceived the research and designed the experiments. L.Z. synthesized the material. L.K.I. and D.O. performed the experiments. L.K.I. and S.D.M. analyzed the data. N.R., S.E.W., and L.F.W. performed the DFT calculations. R.M. and K.G.S. performed the MD simulations. L.K.I., S.D.M, N.R., E.N.A., R.M., L.Z., D.O., S.W., K.G.S., L.F.W., and M.F.T. co-wrote the manuscript. All authors discussed the results and contributed to the manuscript.

Declaration of Interests

References:

[1] Wu, C., Yang, Y., Zhang, Y., Xu, H., He, X., Wu, X., and Chou, S. (2024). Hard carbon for sodium-ion batteries: progress, strategies and future perspective. Chem. Sci., 15, 6244-6268. 10.1039/D4SC00734D.

[2] Hirsh, H.S., Li, Y., Tan, D.H.S., Zhang, M., Zhao, E., and Meng, Y.S. (2020). Sodium-ion Batteries Paving the Way for Grid Energy Storage. Adv. Energy Mater., 10. 10.1002/aenm.202001274.

[3] Slater, M.D., Kim, D., Lee, E., and Johnson, C.S. (2013). Sodium-ion Batteries. Adv. Funct. Mater., 23(8), 947–958. 10.1002/adfm.201200691.

[4] Delmas, C. (2018). Sodium and Sodium-ion Batteries: 50 Years of Research. Adv. Energy Mater., 8(17). 10.1002/aenm.201703137.

[5] Hwang, JY., Myung, ST., and Sun, YK. (2017). Sodium-ion batteries: present and future. Chem. Soc. Rev., 46(12), 3529-3614. 10.1039/C6CS00776G.

[6] Tarascon, J.-M. (2020). Na-ion versus Li-ion Batteries: Complementarity Rather than Competitiveness. Joule, 1616-1620. 10.1016/j.joule.2020.06.003.

[7] Stevens, D.A., and Dahn, J.R. (2000). High Capacity Anode Materials for Rechargeable Sodium-Ion Batteries. J. Electrochem. Soc., 147, 1271. 10.1149/1.1393348.

[8] Yamamoto, H., Muratsubaki, S., Kubota, K., Fukunishi, M., Watanabe, H., Kim, J., and Komaba, S. (2018). Synthesizing higher-capacity hard-carbons from cellulose for Na- and K-ion batteries. J. Mater. Chem. A, 6, 16844-16848. 10.1039/C8TA05203D.

[9] Li, Y., Hu, Y.-S., Titirici, M.-M., Chen, L., and Huang, X. (2016). Hard Carbon Microtubes Made from Renewable Cotton as High-Performance Anode Material for Sodium-Ion Batteries. Adv. Energy Mater., 6, 1600659. 10.1002/aenm.201600659.

[10] Bai, P., He, Y., Zou, X., Zhao, X., Xiong, P., and Xu, Y. (2018). Elucidation of the Sodium-Storage Mechanism in Hard Carbons. Adv. Energy Mater., 8. 10.1002/aenm.201703217.

[11] Sun, N., Guan, Z., Liu, Y., Cao, Y., Zhu, Q., Liu, H., Wang, Z., Zhang, P., and Xu, B. (2019). Extended "Adsorption–Insertion" Model: A New Insight into the Sodium Storage Mechanism of Hard Carbons. Adv. Energy Mater., 9. 10.1002/aenm.201901351.

[12] Jin, Y., Sun, S., Ou, M., Liu, Y., Fan, C., Sun, X., Peng, J., Li, Y., Qiu, Y., Wei, P., Deng, Z., Xu, Y., Han, J., and Huang, Y. (2018). High-Performance Hard Carbon Anode: Tunable Local Structures and Sodium Storage Mechanism. ACS Appl. Energy Mater., 1(5), 2295-2305. 10.1021/acsaem.8b00354.

[13] Li, Z., Bommier, C., Chong, Z.S., Jian, Z., Surta, T.W., Wang, X., Xing, Z., Neuefeind, J.C., Stickle, W.F., Dolgos, M., Greaney, P.A., and Ji, X. (2017). Mechanism of Na-Ion Storage in Hard Carbon Anodes Revealed by Heteroatom Doping. Adv. Energy Mater., 7. 10.1002/aenm.201602894.

[14] Ding, J., Wang, H., Li, Z., Kohandehghan, A., Cui, K., Xu, Z., Zahiri, B., Tan, X., Lotfabad, E.M., Olsen, B.C., and Mitlin, D. (2013). Carbon nanosheet frameworks derived from peat moss as high performance sodium ion battery anodes. ACS Nano, 7, 12, 11004–11015. 10.1021/nn404640c.

[15] Lotfabad, E.M., Ding, J., Cui, K., Kohandehghan, A., Kalisvaart, W.P., Hazelton, M., and Mitlin, D. (2014). High-density sodium and lithium ion battery anodes from banana peels. ACS Nano, 8(7), 7115-7129. 10.1021/nn502045y.

[16] Bommier, C., Surta, T.W., Dolgos, M., and Ji, X. (2015) New Mechanistic Insights on Na-Ion Storage in Nongraphitizable Carbon. Nano Lett., 15 (9), 5888-5892. 10.1021/acs.nanolett.5b01969.

[17] Reddy, M.A., Helen, M., Groß, A., Fichtner, M., and Euchner, H. (2018). Insight into Sodium Insertion and the Storage Mechanism in Hard Carbon. ACS Energy Lett., 3(12), 2851-2857. 10.1021/acsenergylett.8b01761.

[18] Stevens, D.A., and Dahn, J.R. (2001). The Mechanisms of Lithium and Sodium Insertion in Carbon Materials. J. Electrochem. Soc., 148. 10.1149/1.1379565.

[19] Komaba, S., Murata, Q., Ishikawa, T., Yabuuchi, N., Ozeki, T., Nakayama, T., Ogata, A., Gotoh, K., and Fujiwara, K. (2011). Electrochemical Na Insertion and Solid Electrolyte Interphase for Hard-Carbon Electrodes and Application to Na-Ion Batteries. Adv. Funct. Mater., 21, 3859-3867. 10.1002/adfm.201100854.

[20] Weaving, J.S., Lim, A., Millichamp, J., Neville, T.P., Ledwoch, D., Kendrick, E., McMillan, P.F., Shearing, P.R., Howard, C.A., and Brett, D.J.L. (2020). Elucidating the Sodiation Mechanism in Hard Carbon by Operando Raman Spectroscopy. ACS Appl. Energy Mater., 3(8), 7474-7484. 10.1021/acsaem.0c00867.

[21] Morikawa, Y., Nishimura, S.-I., Hashimoto, R.-I., Ohnuma, M., and Yamada, A. (2020). Mechanism of Sodium Storage in Hard Carbon: An X-Ray Scattering Analysis. Adv. Energy Mater., 10. 10.1002/aenm.201903176.

[22] Li, Y., Vasileiadis, A., Zhou, Q., Lu, Y., Meng, Q., Li, Y., Ombrini, P., Zhao, J., Chen, Z., Niu, Y., et al. (2024). Origin of fast charging in hard carbon anodes. Nat. Energy, 9, 134–142. 10.1038/s41560-023-01414-5.

[23] Saju, K.S., Chattopadhyay, S., Xu, J., Alhashim, S., Pramanik, A., and Ajayan, P.M. (2024). Hard carbon anode for lithium-, sodium-, and potassium-ion batteries: Advancement and future perspective. Cell Rep. Phys. Sci., 5, 3. 10.1016/j.xcrp.2024.101851.

[24] Stratford, J.M., Kleppe, A.K., Keeble, D.S., Chater, P.A., Meysami, S.S., Wright, C.J., Barker, J., Titirici, M.-M., Allan, P.K., and Grey, C.P. (2021). Correlating Local Structure and Sodium Storage in Hard Carbon Anodes: Insights from Pair Distribution Function Analysis and Solid-State NMR. J. Am. Chem. Soc., 143(35), 14274-14286. 10.1021/jacs.1c06058.

[25] Kitsu Iglesias, L., Antonio, E.N., Martinez, T.D., Zhang, L., Zhuo, Z., Weigand, S.J., Guo, J., and Toney, M.F. (2023). Revealing the Sodium Storage Mechanisms in Hard Carbon Pores. Adv. Energy Mater., 13. 10.1002/aenm.202302171.

[26] Wang, C., Thenuwara, A.C., Luo, J., Shetty, P.P., McDowell, M.T., Zhu, H., Posada-Perez, S., Xiong, H., Hautier, G., and Li, W. (2022). Extending the low-temperature operation of sodium metal batteries combining linear and cyclic ether-based electrolytes. Nat. Commun., 13, 4934. 10.1038/s41467-022-32606-4

[27] Petkov, V., Difrancesco, R.G., Billinge, S.J.L., Acharya, M., and Foley, H.C. (1999). Local Structure of Nanoporous Carbons. Philosophical Magazine B, 79(10), 1519–1530. 10.1080/13642819908218319.

[28] Gomez-Martin, A., Martinez-Fernandez, J., Ruttert, M., Winter, M., Placke, T., and Ramirez-Rico, J. (2019). Correlation of Structure and Performance of Hard Carbons as Anodes for Sodium Ion Batteries. Chem. Mater., 31(18), 7288-7299. 10.1021/acs.chemmater.9b01768.

[29] Mathiesen, J.K., Väli, R., Härmas, M., Lust, E., Fold von Bulow, J., Jensen, K.M.Ø., and Norby, P. (2019). Following the In-Plane Disorder of Sodiated Hard Carbon through Operando Total Scattering. J. Mater. Chem. A, 7(19), 11709−11717. doi.org/10.1039/C9TA02413A.

[30] Olsson, E., Cottom, J., Au, H., Guo, Z., Jensen, A.C.S., Alptekin, H., Drew, A.J., Titirici, M.-M., and Cai, Q. (2020). Elucidating the Effect of Planar Graphitic Layers and Cylindrical Pores on the Storage and Diffusion of Li, Na, and K in Carbon Materials. Adv. Func. Mater., 30. 10.1002/adfm.201908209.

[31] Olsson, E., Chai, G., Dove, M., and Cai, Q. (2019). Adsorption and migration of alkali metals (Li, Na, and K) on pristine and defective graphene surfaces. Nanoscale, 11, 5274-5284. 10.1039/C8NR10383F.

[32] Nixon, D.E., and Parry, G.S. (1969). The Expansion of the Carbon-Carbon Bond Length in Potassium Graphites. J. Phys. C: Solid State Phys., 2(10), 1732−1741. 10.1088/0022-3719/2/10/305.

[33] Stankovich, S., Dikin, D.A., Piner, R.D., Kohlhaas, K.A., Kleinhammes, A., Jia, Y., Wu, Y., Nguyen, S.T., and Ruoff, R.S. (2007). Synthesis of graphene-based nanosheets via chemical reduction of exfoliated graphite oxide. Carbon, 45, 7, 1558-1565. 10.1016/j.carbon.2007.02.034.

[34] Bommier, C., Ji, X., and Greaney, P.A. (2019). Electrochemical Properties and Theoretical Capacity for Sodium Storage in Hard Carbon: Insights from First Principles Calculations. Chem. Mater., 31, 658–677. 10.1021/acs.chemmater.8b01390.

[35] Kresse, G., and Hafner, J. (1993). *Ab initio* molecular dynamics for liquid metals. Phys. Rev. B, 47, 558. 10.1103/PhysRevB.47.558.

[36] Kresse, G., and Hafner, J. (1994). *Ab initio* molecular-dynamics simulation of the liquid-metal–amorphous-semiconductor transition in germanium. Phys. Rev. B, 49, 14251. 10.1103/PhysRevB.49.14251.

[37] Kresse, G., and Furthmüller, J. (1996). Efficiency of ab-initio total energy calculations for metals and semiconductors using a plane-wave basis set. Comput. Mat. Sci., 6, 15-50. 10.1016/0927-0256(96)00008-0.

[38] Kresse, G., and Furthmüller, J. (1996). Efficient iterative schemes for ab initio total-energy calculations using a plane-wave basis set. Phys. Rev. B, 54, 11169. 10.1103/PhysRevB.54.11169.

[39] Kresse, G., and Joubert, D. (1999). From ultrasoft pseudopotentials to the projector augmented-wave method. Phys. Rev. B, 59, 1758. 10.1103/PhysRevB.59.1758.

[40] Perdew, J.P., Burke, K., and Ernzerhof, M. (1996). Generalized Gradient Approximation Made Simple. Phys. Rev. Lett., 78, 1396. 10.1103/PhysRevLett.77.3865.

[41] Monkhorst, H.J., and Pack, J.D. (1976). Special points for Brillouin-zone integrations. Phys. Rev. B, 13, 5188. 10.1103/PhysRevB.13.5188.

[42] Grimme, S., Ehrlich, S., and Goerigk, L. (2011). Effect of the damping function in dispersion corrected density functional theory. J. Comput. Chem., 32. 10.1002/jcc.21759.